A COUPLED CFD–DEM NUMERICAL STUDY OF THE AERODYNAMIC SORTING OF *ZANTHOXYLUM BUNGEANUM* SHELLS AND SEED-BEARING PARTICLES
/
基于 CFD-DEM 耦合的红花椒果壳与带籽椒粒气动分选数值模拟研究

Ruiqiang XU [1], Zhongbin LIU *[1], Hongwei XIAO [2], Chunglim LAW [3], Fengkui XIONG *[1, 2]
[1] College of Mechanical Engineering, Sichuan University of Science and Engineering, Yibin, Sichuan 644000, P. R China;
[2] College of Engineering, China Agricultural University, Beijing 100080, P. R. China;
[3] Taylor's University, Subang Jaya, 47500, Malaysia.
Corresponding author: Zhongbin Liu; E-mail: liuzb@suse.edu.cn; Fengkui Xiong; E-mail: xfk763101899@126.com
DOI: https://doi.org/10.35633/inmateh-79-45

Keywords: *Zanthoxylum bungeanum, aerodynamic sorting, computational fluid dynamics, discrete element method*

ABSTRACT
This study presents a particle-scale coupled CFD–DEM numerical approach for elucidating aerodynamic sorting mechanisms and optimizing process parameters. Non-spherical particle models were developed to represent the geometric and physical differences between shells and seed-bearing particles. The Stokes number, which characterizes the balance between aerodynamic drag and particle inertia, was identified as the primary determinant of sorting performance. Under the optimized conditions, a primary airflow velocity of 8.4 m/s, a secondary airflow velocity of 7.85 m/s, and a feed mass flow rate of 80 g/s, the system achieved a shell purity of 95.3% and a recovery rate of 58.2% when processing feedstock with an initial shell content of 5%. The results further revealed an inherent trade-off between purity and recovery. These findings provide a theoretical and numerical basis for the design and optimization of aerodynamic sorting equipment.

摘要
本研究提出了一种基于颗粒尺度的 CFD-DEM 耦合数值模拟方法，旨在阐明气动分选机制并优化工艺参数。建立了非球体模型，以表征果壳与种子团聚体之间的几何和物理差异。研究发现，表征气动阻力与惯性平衡的斯托克斯数是分选性能的核心决定因素。在最优条件下（主气流速度 8.4 m/s，副气流速度 7.85 m/s，进料速率 80 g/s），以初始纯度为 5%的原料为进料，可获得 95.3%的壳体纯度和 58.2%的回收率。研究揭示了纯度与回收率之间固有的权衡关系，为分选设备的设计与优化提供了理论和数据支持。

INTRODUCTION
Zanthoxylum bungeanum serves as a vital spice and economic crop in China, celebrated for its unique pungent and numbing flavor, which primarily derives from the volatile oils and alkyl amides found in its pericarp *(Shi et al., 2025)*. Post-harvest processing typically results in a mixture of hollow shells and seed-bearing particles after threshing. Given the significant differences in flavor profiles, economic value, and suitability for downstream processing between the shells and seed-bearing particles, efficient separation is essential for improving product purity and market value *(Mutinda et al., 2023)*. Conventional sieving methods are ineffective due to the overlapping size and density ranges of these components. However, the distinct shapes and aerodynamic properties of the shells and seed-bearing particles offer a promising opportunity for separation through airflow classification, a precise sorting technique well-suited for this fine separation task *(Stepanenko et al., 2022)*.

Aerodynamic sorting is a clean, efficient technology widely used for cleaning and grading agricultural materials. Its effectiveness depends on the interaction between material properties (size, shape, density, terminal velocity) and airflow parameters *(Zhu et al., 2021)*. Particle shape significantly influences aerodynamic behavior; non-spherical particles behave differently from spherical ones *(Ulusoy et al., 2023)*. *Zanthoxylum bungeanum* shells and seed-bearing particles are typical non-spherical granules. Their separation involves complex gas-solid interactions that traditional empirical design methods fail to adequately explain at the particle scale. In recent years, coupled CFD–DEM has become a robust tool for investigating complex multiphase flows. DEM effectively captures the geometry, contact mechanics, and motion of non-spherical particles *(Ma et al., 2022)*.

Representative applications include: safflower petal cleaning, where high-fidelity shape models visualized trajectory separation driven by mass and aerodynamic differences *(Hu et al., 2021)*; sunflower seed shell-kernel separation, optimizing air channel parameters *(Guan et al., 2025);* rice cleaning, using multi-sphere models to study airflow velocity and inclination angle effects on impurity and loss rates *(Ma et al., 2020)*.

Accurate CFD–DEM simulations rely on precise particle models and contact parameters. Foundational studies have established the fundamental physical properties of *Zanthoxylum bungeanum* particles and their contact parameters with common engineering materials via experiments and calibration *(Wang et al., 2023; Zhang et al., 2022)*, providing a reliable particle-scale mechanical basis. For non-spherical particles, the parametric function method offers a flexible, efficient approach to construct complex non-convex geometries, especially suitable for biological particles with concave features *(Zhao et al., 2021)*. Despite advancements, systematic CFD–DEM studies on the motion, separation dynamics, and mechanisms of *Zanthoxylum bungeanum* shell-seed mixtures in tailored airflow fields remain lacking. To address this gap, the present study employs parametric proxy models based on superquadric surfaces *(Xu et al., 2025)* to capture critical geometric differences between shells and seed-bearing particles. High-fidelity discrete–element simulations are achieved by three-dimensional modeling in SolidWorks and subsequently importing them into rocky DEM software.

MATERIAL AND METHODS

GOVERNING EQUATIONS AND NUMERICAL METHODOLOGY

In the simulation herein, air was simply modelled as an incompressible ideal gas *(Xiao et al., 2022)*. The overall initial conditions of the system assumed homogeneous air distribution, neglecting other secondary factors such as dust generation, particle shrinkage, and chemical reactions. The gas phase was treated as a single continuous medium, with its flow governed by the continuity and momentum equations solved within a standard Eulerian framework. Momentum exchange between the gas and solid phases was incorporated through appropriate interphase momentum exchange terms *(Wu et al., 2025)*. Utilizing the widely adopted fluent-rocky coupled strategy, this model employed the Eulerian multiphase model in commercial fluent to resolve gas flow, while simultaneously the Discrete Element Method (DEM) in rocky was used to track the motion of individual particles. This robust integrated approach facilitated a high-fidelity coupled simulation of the gas-solid two-phase system.

The mass conservation equation is expressed as:

$$\frac{\partial}{\partial t}\left(\rho_g \theta_g\right) + \nabla \cdot \left(\rho_g \theta_g u_g\right) = 0 \tag{1}$$

where: u_g is the fluid velocity vector, m/s; ρ_g is the gas-phase density, kg/m^3; θ_g is the gas phase volume fraction, %.

The momentum conservation equation is:

$$\frac{\partial}{\partial t}\left(\rho_g \theta_g u_g\right) + \nabla \cdot \left(\rho_g \theta_g u_g u_g\right) = -\nabla P + \nabla \cdot \left(\theta_g \tau_g\right) + \rho_g \theta_g g + M \tag{2}$$

where: P is the static pressure, Pa; τ_g is the gas-phase viscous stress tensor, Pa; g is the gravitational acceleration vector, m/s²; M is the gas-solid interphase momentum exchange rate per unit volume, N/m³.

For a Newtonian fluid, the viscous stress tensor can be expressed as:

$$\tau_g = \mu_g \left[\nabla u_g + \left(\nabla u_g\right)^T\right] - \frac{2}{3}\mu_g \left(\nabla \cdot u_g\right) I \tag{3}$$

where: u_g is the gas dynamic viscosity.

The interphase momentum exchange rate is given by the following equation:

$$M = -\frac{1}{V_{cell}} \sum_{l=1}^{n} F_{d,l} \tag{4}$$

where: $F_{d,l}$ is the drag force acting on particle i, N; V_{cell} is the computational cell volume, m^3.

In multiphase flow systems, the motion of the particulate phase can be described using a probability distribution function in conjunction with the Liouville equation *(Domínguez-Vázquez et al., 2024)*. For the particulate phase of *Zanthoxylum bungeanum*, a distribution function $f(x, u_p, p_p, V_p, t)$ is defined, where x, u_p, p_p, V_p and t represent the particle's spatial position, velocity vector, density, volume, and time. This function fully defines the probabilistic distribution state of the particles in phase space, and the system is closed by solving the following Liouville equation:

$$\frac{\partial f}{\partial t} + \nabla_x \cdot (f u_p) + \nabla_{u_p} \cdot (f a_p) = 0 \quad (5)$$

where: a_p is the particle acceleration, m/s², determined by the net force acting on the particle according to Newton's second law.

In the simulation, air enters the chamber and penetrates the porous particle layer. Confined by walls and outlet geometry, fully developed turbulence forms. Due to short inlet–outlet distance and narrow flow gaps, a complex flow structure with recirculation and vortices emerges *(Echendu et al., 2011)*. To simulate this turbulence, the Realizable k-ε model *(Gong et al., 2025)* is used to close the Reynolds-averaged Navier-Stokes equations. This model computes turbulent viscosity by solving transport equations for turbulent kinetic energy (k) and dissipation rate (ε).

$$\mu_t = \rho_g C_\mu \frac{\kappa^2}{\epsilon} \quad (6)$$

where: C_μ is no longer a constant. The empirical constants in the model take the following standard values: $C_{1\epsilon}$=1.44, C_2=1.9, σ_k=1.0, σ_ϵ=1.2.

SIMULATION SETUP

Computational Model and Parameter Specification

To investigate the motion patterns of particles during air-classification, a model of the classification apparatus measuring 397 mm in length, 110 mm in width and 309 mm in height was constructed; the apparatus is equipped with one feed inlet, two air inlets, two air outlets, three collection chambers and two classification stages (Fig. 1a). The two air inlets, with a combined length of 110 mm and a width of 76 mm, are inclined at an angle of 46.7° relative to the horizontal plane. They consist of a series of slotted inlets, each 2 mm wide and spaced 0.1 mm apart (Fig. 1b). They are made of the same material as the apparatus casing, and the width of the inlets is smaller than that of the *Zanthoxylum bungeanum* grains.

During the sorting process, the particles fall under the influence of gravity along a deflector plate inclined at an angle of 45° to the horizontal. The first stage performs preliminary separation, increasing the shell proportion entering the second stage. After first-stage separation, most seed-bearing particles and a few shells enter Collection Bin 1. The remaining mixture proceeds to the second stage for fine sorting. Ultimately, Collection Bin 3 yields predominantly shells, while Bin 2 contains a mixture.

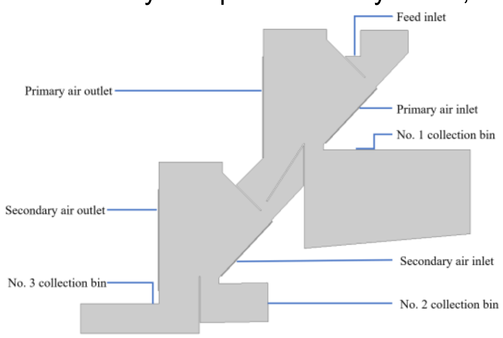

(a) general schematic diagram

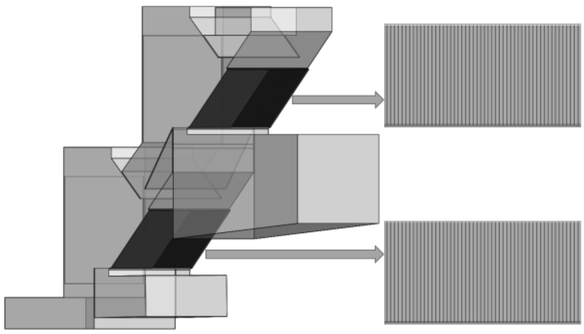

(b) close-up

Fig. 1 - Schematic of the sorting device model

ANSYS Fluent was used to establish a continuous-phase flow field; *Zanthoxylum bungeanum* particles were generated using the 3D modelling software SolidWorks and imported into Rocky for DEM simulation. In the numerical simulation, the continuous-phase CFD calculations were performed on a 12th-generation Intel® Core™ i5-12490F processor with 16 GB of system memory. The discrete-phase DEM calculations were performed on an NVIDIA GeForce RTX 4060 graphics card with 8 GB of dedicated GDDR6 video memory. The CFD simulation for the gas phase took approximately 10 minutes, using the 'Automatic' time-step method, a time scaling factor of 0.1, and 200 iterations; the DEM simulation for the solid phase took approximately 74 hours, with a simulation duration of 4 s, with a time interval of 0.01 s. Since the volume fraction of the particulate phase is 0.068%, constituting a dilute gas-solid two-phase flow, and given the simulation time constraints, the gas-phase separation process was simulated using the Fluent-Rocky unidirectional coupling method *(Guan et al., 2025; Luo et al., 2020)*. The gas-phase governing equations are discretized by the finite volume method with the SIMPLE algorithm and second-order upwind scheme, and the realizable k-ε model is used for turbulence closure. For the discrete particle phase, the soft-sphere contact model is applied to calculate inter-particle and particle-wall contact forces, and particle kinematics are updated by an explicit time integration scheme in the Lagrangian framework.

The coefficient of restitution, coefficient of static friction and coefficient of rolling friction between *Zanthoxylum bungeanum* particles are 0.378, 0.56 and 0.0143, respectively. As the rolling coefficient of friction between *Zanthoxylum bungeanum* particles and galvanized steel sheet is relatively low (0.168) *(Zhang et al., 2022)*, this material was selected for the device walls. In this simulation, the density of the *Zanthoxylum bungeanum* was set at 997 kg/m³, with a Poisson's coefficient of 0.168 and a Young's modulus of 1.568 × 10^7 Pa *(Wang et al., 2023)*. The density of galvanized steel was 7,850 kg/m³, with a Poisson's coefficient of 0.3 and a Young's modulus of 206 GPa *(Gu et al., 2024)*.

Rationale and Parameterization of Particle Geometry Simplification

This study investigates the sorting process of *Zanthoxylum bungeanum* shells and seed-bearing particles. The total feed mass is 50 g, and the initial shell mass fraction is 5%. The material enters via the feed inlet at the top of the apparatus, with a total mass flow rate of 50 g/s to 120 g/s; the feed falls freely without any initial velocity. Air enters through two air inlets at a velocity of 6.85 m/s to 8.85 m/s, which corresponds to a volumetric flow rate of 206.16 m³/h to 266.35 m³/h. In the coupled CFD–DEM simulations, physics-oriented proxy models are used to balance computational efficiency and fidelity *(Ma et al., 2022)*.

Geometry is simplified based on dominant aerodynamic sorting mechanisms to capture the separation of shells from seed-bearing particles. Despite similar density, shells and seed-bearing particles behave differently due to geometry-induced forces. In transverse flow, trajectory reflects the Stokes number (drag vs. inertia), set by the volume-to-mass ratio linking geometry to dynamics *(Zhao et al., 2024)*. Based on mechanistic analysis, the volume-to-mass ratio is identified as the dominant parameter controlling shell–seed separation. To capture this difference in the model, two critical geometric features are abstracted: (1) the hollow, thin-walled shell structure, which causes the mass difference; (2) the aperture size, which affects the maximum projected area and thus the drag coefficient. Guided by this analysis, parametric proxy models are established *(Michaelides et al., 2023)*: pepper shells are modeled as hollow, thin-walled structures with large apertures to achieve a high volume-to-mass ratio; seed-bearing particles are modeled as composite structures with small apertures and internal spherical seed fillings to obtain a low volume-to-mass ratio. Geometric parameters are determined via sensitivity analysis from a preliminary study to maximize the difference in dynamic behavior.

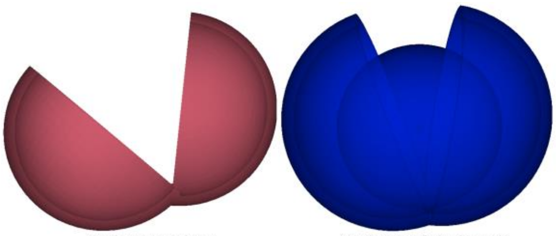

Fig. 2 - Geometric models of the particles

RESULTS AND DISCUSSION

Particle Distribution and Separation Mechanism

Recovery and purity are in conflict *(Lundin et al., 2024)*; for *Zanthoxylum bungeanum*, high purity is demanded. We thus maximize shell recovery in Bin 3 at >90% purity, acknowledging that relaxing purity boosts yield. To separate shells from seed-bearing particles, simulations employed distinct particle sizes/shapes *(Li et al., 2024)*. Despite similar density, volume/mass differences cause distinct free-fall behaviors. In airflow, particles experience gravity, drag, and inertia. Shells have a high volume-to-mass ratio and are easily entrained; seed-bearing particles have a low ratio, leading to stronger sedimentation and shorter migration *(Zhou et al., 2023)*. Adjusting airflow velocity amplifies this ratio's effect on trajectories, achieving separation. CFD–DEM validation clarifies sorting physics, enabling rational parameter selection over empirical optimization.

Effect of Secondary Airflow Velocity on Sorting Performance

Secondary airflow velocity was a key parameter governing both the flow-field characteristics and separation performance within the second-stage classification zone. By analyzing the flow-field contour maps (Fig. 4) and particle-distribution patterns (Fig. 3) at different airflow velocities, the underlying separation mechanism was clarified.

At low velocities (6.85–7.35 m/s), the low-velocity regions (cool colors) was uniform with a gentle gradient and lacks a high-speed core, indicating insufficient kinetic energy to penetrate the particle bed. At the optimal velocity (7.85 m/s), a stable, well-defined high-speed pathway formed without recirculation or vortices, concentrating flow energy along the separation path for highly selective sorting. At higher velocities (8.35–8.85 m/s), the flow became chaotic, with localized high-speed patches and recirculation vortices, where excess kinetic energy caused instability, dissipation, and flow separation. At low velocities, insufficient drag yielded high Stk; particle motion was inertia-dominated. Shells were not conveyed to Bin 3, causing low recovery; seed-bearing particles settled normally. Bin 3 purity remained acceptable, but the efficiency was poor. At the optimal velocity (7.85 m/s), drag and inertia were balanced: shells were carried into Bin 3, while seed-bearing particles settled into Bin 1, achieving separation. At high velocities, excessive drag caused an "over-bearing" effect, entraining seed-bearing particles into Bin 3 and reducing its purity to 52.5%. The Stokes number difference between the two particle types diminished; their dynamic responses converge, and separation selectivity was lost. Thus, secondary airflow velocity governed particle trajectories via the Stokes number by modulating flow-field structure and gas-solid momentum transfer.

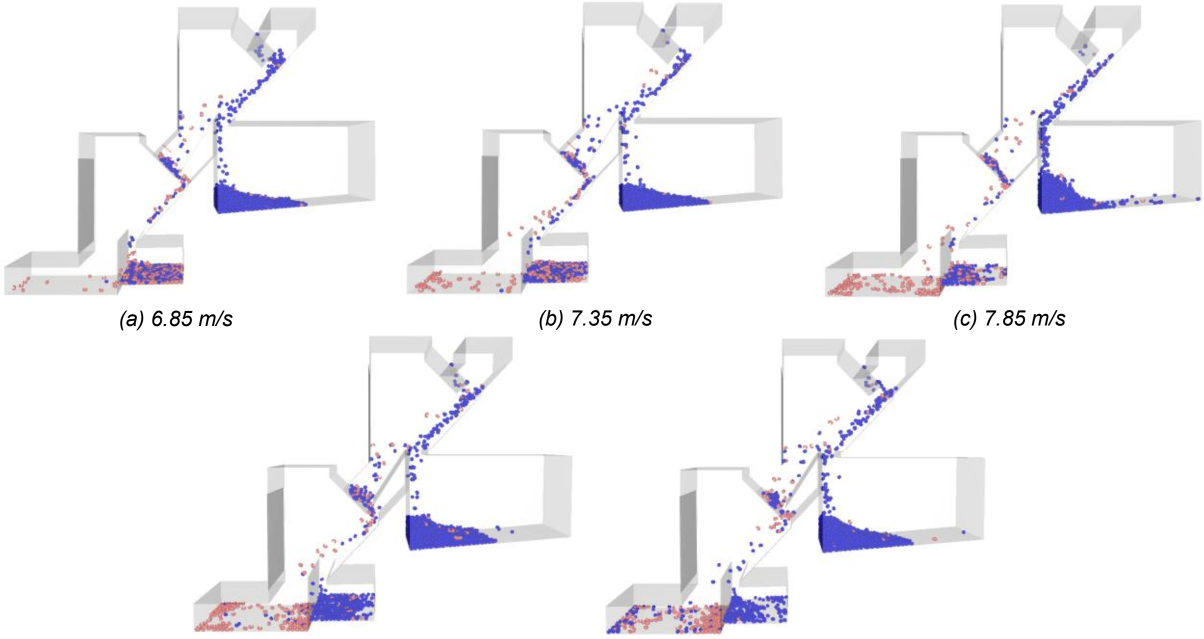

(a) 6.85 m/s (b) 7.35 m/s (c) 7.85 m/s

(d) 8.35 m/s (e) 8.85 m/s

Fig. 3 - Distribution Patterns of Pepper Particles

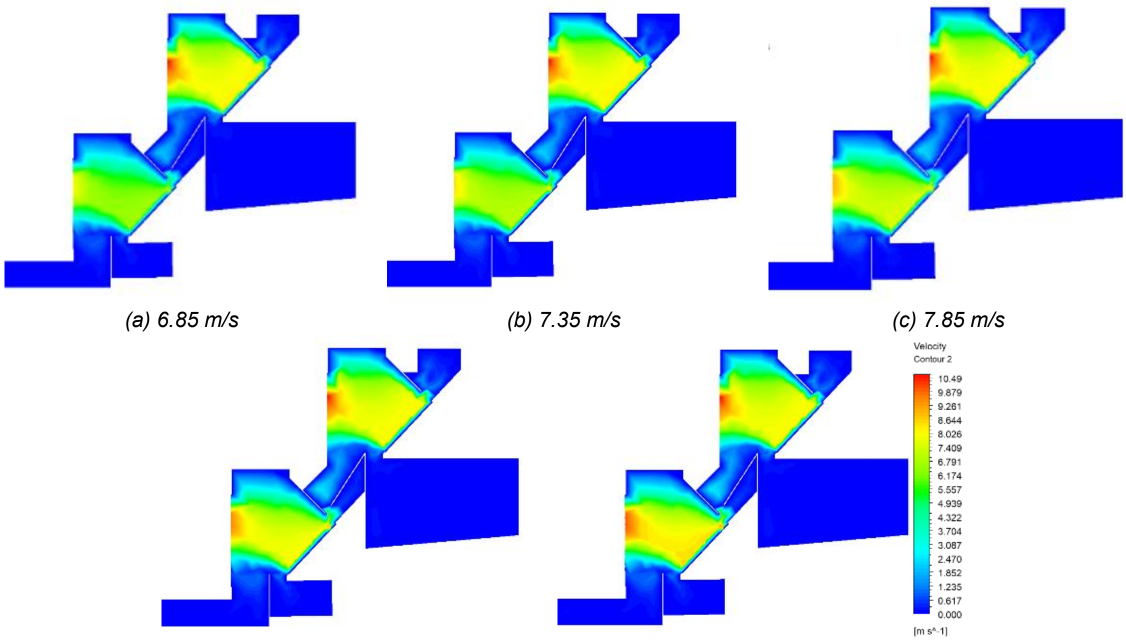

(a) 6.85 m/s (b) 7.35 m/s (c) 7.85 m/s

(d) 8.35 m/s (e) 8.85 m/s

Fig. 4 - Contour of secondary airflow velocity

As shown in Fig. 5, with increasing secondary airflow velocity, shell purity in Bin 3 first rose then declined (with a sharper drop at high speeds), while purity in Bin 2 decreased continuously. Although excessively low airflow velocity helped prevent heavier seed-bearing particles from entering Bin 3, it also reduced the overall inflow of pepper shells, resulting in low shell purity in this bin.

Notably, seed-bearing particles had a larger mass and settling velocity, and even a small amount of their potential contamination could markedly reduce the purity of pepper shells. Notably, Bin 2 purity remained below 30%, whereas Bin 3 consistently exceeded 50%, confirming effective enrichment by the secondary airflow stream. At an airflow velocity of 7.35 m/s, the shell purity in Bin 3 reached a maximum of 96.6%, whereas the recovery rate was only 25.7% (Fig. 6). When the airflow velocity increased to 7.85 m/s, purity decreased slightly to 91.8%, while recovery increased substantially to 59.7%. These results clearly demonstrate the inherent trade-off between purity and recovery, indicating that system optimization must balance these competing objectives. The findings are consistent with the fundamental principles of aerodynamic classification and provide previously unavailable particle-scale mechanistic insights into the separation behavior of *Zanthoxylum bungeanum*. The validated CFD–DEM framework therefore offers a robust tool for the rational design and optimization of sorting equipment for similarly complex agricultural materials.

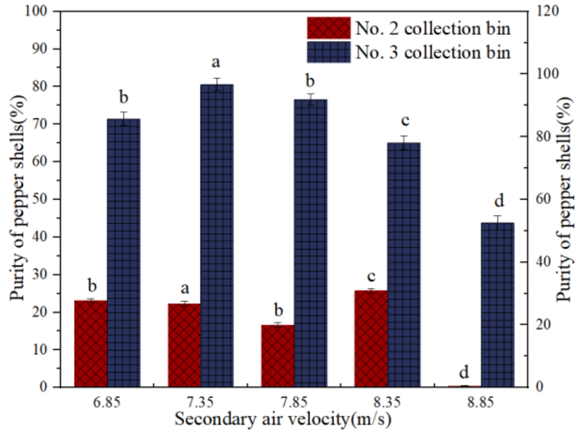

Fig. 5 - Purity of Pepper Shells in Different Collection Bins

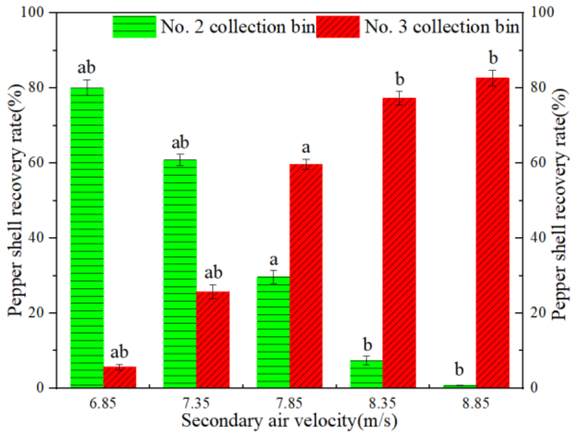

Fig. 6 - Recovery Rate of Pepper Shells in Different Collection Bins

As shown in Fig. 6, Bin 2 achieved the highest shell recovery at an airflow velocity of 6.85 m/s, reaching 80.1%, although shell purity remained below 25%. At 8.85 m/s, shell recovery in Bin 3 increased to 82.7%; however, the entrainment of seed-bearing particles reduced shell purity to a minimum of 52.5%. These results indicate that increasing airflow velocity enhances shell recovery but may simultaneously reduce product purity because of greater carryover of non-target particles. Figs. 5 and 6 further quantify the effect of secondary airflow velocity. Increasing the velocity from 7.35 to 7.85 m/s reduced shell purity in Bin 3 from 96.6% to 91.8%, while markedly increasing recovery from 25.7% to 59.7%, resulting in a more favorable overall separation performance at 7.85 m/s. This behavior can be interpreted in terms of Stokes number (Stk) optimization *(Farooq et al., 2023)*. At 7.85 m/s, Stk for the shells was much less than 1, indicating fluid-dominated motion, whereas Stk for the seed-bearing particles was close to or greater than 1, indicating inertia-dominated motion. Maximizing the difference in Stk between the two particle groups therefore promotes efficient aerodynamic separation.

At an airflow velocity of 8.85 m/s, shell recovery increased to 82.7%, whereas purity decreased sharply to 52.5%. This indicates that excessive airflow velocity reduces the difference in Stokes number between the two particle groups, thereby weakening separation selectivity. Accordingly, 7.85 m/s was identified as the optimal velocity for balancing recovery and purity. Under this condition, Bin 3 achieved a shell recovery of 59.7% and a purity of 91.8%. Aerodynamic drag enabled highly selective separation while minimizing the carryover of seed-bearing particles. The less-than-maximum recovery may be attributed to shells with aerodynamic characteristics close to the separation threshold, as well as particle losses caused by interparticle collisions and unfavorable initial positions. These limitations could be addressed in future studies through multistage cascade separation or improved flow-field uniformity.

By achieving a purity of 91.8% and a recovery of 59.7%, the separation of *Zanthoxylum bungeanum* shells from seed-bearing particles was successfully accomplished, despite their similar physical properties. This result outperforms traditional sieving processes (which are prone to blockages and are inefficient), demonstrating the feasibility and superiority of aerodynamic sorting in this application. The CFD–DEM framework elucidates the mechanisms at the particle scale and provides a predictive tool for optimizing the sorting of other complex agricultural products. A limitation of this study is its focus on single-stage optimization; future research could explore dynamic control or multi-stage integration to further enhance the upper limits of purity and recovery.

Effect of Primary Airflow Velocity on Sorting Performance

The primary airflow provides the initial momentum and performs pre-classification for the entire sorting process. With the secondary airflow velocity fixed at the optimal 7.85 m/s, the influence of the primary airflow velocity was systematically investigated. As shown in Fig. 7, increasing the primary airflow velocity led to a gradual decrease in the purity of pepper shells collected in Bin 3. The underlying cause of this trend can be attributed to a chain reaction in the dynamics: an excessively high primary velocity imparts substantial horizontal initial kinetic energy to the particles, reducing their effective residence time in the first-stage classification zone. The resulting high-energy, high-concentration particle stream then enters the stabilized flow field of the secondary classification zone, where it substantially increases the frequency of interparticle collisions. These interactions promote dynamic agglomeration and ultimately impair separation performance. Therefore, the objective of primary-airflow optimization is not to maximize preliminary separation, but rather to deliver a uniformly distributed feed with moderate kinetic energy to the secondary stage. This is an essential prerequisite for effective fine classification. Unlike studies that evaluate airflow parameters independently, the present analysis reveals the coupling between successive classification stages and highlights the importance of coordinated parameter optimization for overall system performance.

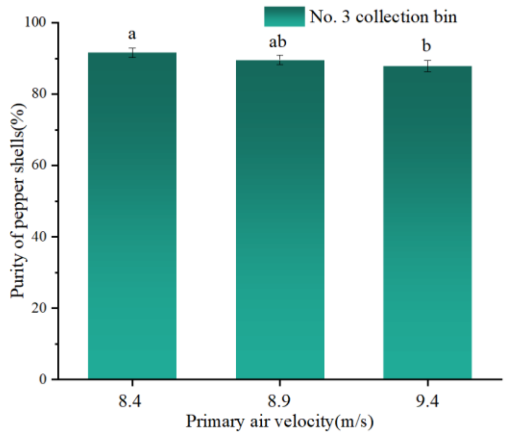

Fig. 7 - Purity of Pepper Shells in Collection Bin 3

Effect of Feed Mass Flow Rate on Sorting Efficiency

Under the optimal airflow conditions, the feed mass flow rate exhibited a trade-off between processing capacity and separation performance. As the feed mass flow rate increased from 64 to 80 g/s (Figs. 8 and 9), shell purity in Bin 3 increased from 91.8% to 95.3%, while recovery decreased slightly from 59.7% to 58.2%. This behavior may be attributed to the higher solid-to-gas ratio at the increased feed rate.

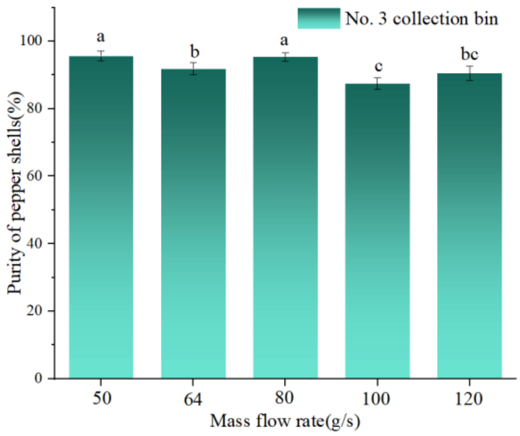

Fig. 8 - Purity of Pepper Shells in Collection Bin 3

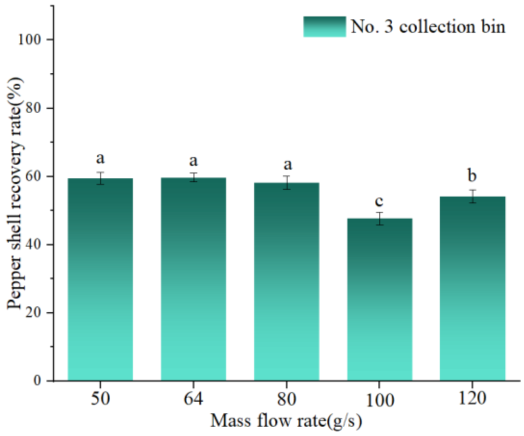

Fig. 9 - Recovery Rate of Pepper Shells in Collection Bin 3

The greater particle concentration intensified interparticle interactions and reduced the average aerodynamic drag acting on individual particles. The consistently high purity observed over the tested range indicates that the fundamental separation mechanism remained effective. Increasing the feed mass flow rate to 80 g/s produced a 25% increase in throughput with only a minor reduction in recovery, representing a favorable engineering compromise. Considering purity, recovery, and processing capacity together, 80 g/s was identified as the optimal feed mass flow rate, yielding a shell purity of 95.3%, a recovery of 58.2%, and the highest throughput tested. In practical applications, overall system performance is more important than maximizing any single indicator. The recovery of 58.2%, achieved without compromising shell purity, represents a balanced and practically relevant operating condition for potential industrial scale-up. These findings demonstrate the value of multi-objective optimization over isolated parameter adjustment and provide a transferable approach for designing sorting systems for similarly complex agricultural materials.

Effect of Feedstock Shell Purity on Sorting Performance

Under the optimal operating conditions—a primary airflow velocity of 8.4 m/s, a secondary airflow velocity of 7.85 m/s, and a feed mass flow rate of 80 g/s—increasing the shell content of the feedstock from 5% to 80% progressively increased shell purity in Collection Bin 3 from 95.3% to 99.5% (Fig. 10). This strong positive relationship demonstrates the substantial influence of particle composition on separation selectivity.

The increase in Bin 3 purity may be explained by changes in the internal particle-flow structure. At a low feedstock shell content of 5%, the target shell fraction is dispersed within a dense background of seed-bearing particles. Although the aerodynamic drag acting on individual shells may be sufficient for separation, frequent collisions with the more abundant seed-bearing particles disturb shell trajectories, preventing some shells from reaching Bin 3 and limiting purity to 95.3%. At higher feedstock shell contents of 60–80%, the particle stream becomes shell-dominated. This collective flow structure may reduce random particle motion, strengthen momentum coupling among shells, and promote more coherent migration of the particle cloud toward Bin 3. Consequently, shell purity approaches 99.5%.

However, increasing the feedstock shell content from 5% to 80% reduced shell recovery in Bin 3 from 58.2% to 49.2% (Fig. 11), revealing an inherent trade-off between purity and recovery. For applications requiring extremely high product purity, a feedstock shell content of at least 60% may be selected, yielding up to 99.5% purity while accepting a recovery of approximately 49.2%. By contrast, when higher recovery is prioritized, a feedstock shell content of 5% provides approximately 95.3% purity and 58.2% recovery. These relationships provide a basis for selecting operating conditions according to different production objectives.

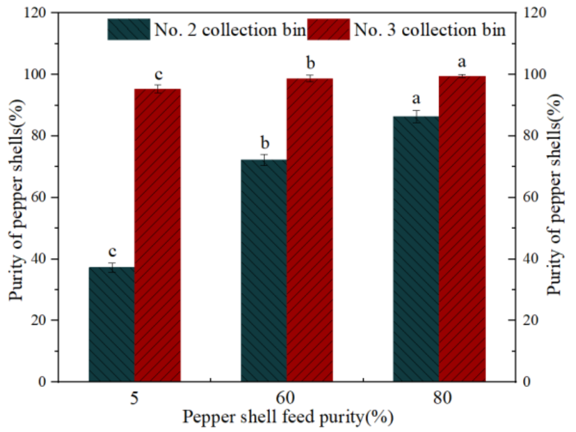

Fig. 10 - Purity of Pepper Shells in Different Collection Bins

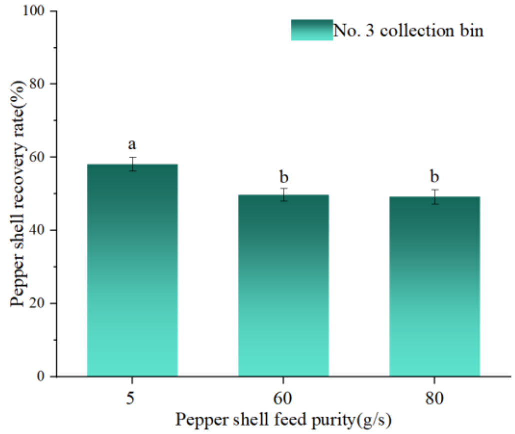

Fig 11 - Recovery Rate of Pepper Shells in Collection Bin 3

CONCLUSIONS

This study elucidated the fundamental mechanism governing the aerodynamic separation of *Zanthoxylum bungeanum* shells from seed-bearing particles. The results demonstrated that separation is primarily controlled by the balance between aerodynamic drag and particle inertia, as characterized by the Stokes number. The substantial difference in Stk between the two particle types, arising from their distinct volume-to-mass ratios and aerodynamic responses, enabled effective segregation.

Systematic parameter analysis showed that the secondary airflow velocity was the most influential factor affecting separation selectivity. At 7.85 m/s, the secondary airflow established a stable flow field in which aerodynamic drag and particle inertia were favorably balanced. The primary airflow mainly conditioned and distributed the incoming particle stream, whereas an excessively high primary airflow velocity disrupted secondary classification. A feed mass flow rate of 80 g/s provided a favorable compromise between throughput and separation performance.

Under the optimized operating conditions of a primary airflow velocity of 8.4 m/s, a secondary airflow velocity of 7.85 m/s, and a feed mass flow rate of 80 g/s, the device processed feedstock containing 5% shells and produced a shell fraction in Collection Bin 3 with a purity of 95.3% and a recovery rate of 58.2%. These results validated the proposed aerodynamic separation mechanism. The study also quantified the inherent trade-off between purity and recovery, thereby providing practical guidance for selecting operating conditions according to different downstream requirements.

Feedstock composition strongly influenced the internal particle-flow regime. Feedstock with a high shell content promoted a shell-dominated flow structure and enhanced collective particle migration toward Collection Bin 3, resulting in shell purities exceeding 99%. However, this improvement was accompanied by a lower recovery rate, indicating that feedstock composition should be considered in the design of upstream pre-sorting processes.

The integrated framework combining physics-based proxy modeling with CFD–DEM simulation successfully reproduced the aerodynamic separation of a non-spherical, multicomponent particle mixture. By linking particle-scale mechanics with system-scale separation performance, the framework provides a reliable basis for the design and optimization of sorting equipment for similarly complex agricultural materials.

ACKNOWLEDGEMENT

This research was funded by the National Natural Science Foundation of China [51876109]; the Sichuan University of Science & Engineering talent introduction project [2025RCZ066] and the Sichuan University of Science & Engineering Innovation Team [SUSE652A010].

REFERENCES

[1] Domínguez-Vázquez, D., Castiblanco-Ballesteros, S. A., Jacobs, G. B., & Tartakovsky, D. M. (2024). High-order Lagrangian algorithms for Liouville models of particle-laden flows. *Journal of Computational Physics*, 515, N.PAG. https://doi.org/10.1016/j.jcp.2024.113281.

[2] Echendu, S. O. S., Belblidia, F., Tamaddon-Jahromi, H. R., & Webster, M. F. (2011). Modelling with viscous and viscoplastic materials under combining and separating flow configurations. *Mechanics of Time-Dependent Materials*, 15(4), 407–428. https://doi.org/10.1007/s11043-011-9161-x.

[3] Elreafay, A. M., Salem, K. M., Abumandour, R. M., Dawood, A. S., & Al Nuaimi, S. (2025). Effect of particle diameter and void fraction on gas–solid two-phase flow: a numerical investigation using the Eulerian–Eulerian approach. *Computational Particle Mechanics*, 12(1), 289–311. https://doi.org/10.1007/s40571-024-00798-9.

[4] Farooq, U., Riaz, H. H., Munir, A., Tariq, A., Zhao, M., & Islam, M. S. (2023). Application of heliox for optimized drug delivery through respiratory tract. *Physics of Fluids*, 35(10). https://doi.org/10.1063/5.0169934.

[5] Gong, M., & Shen, Y. (2025). Study on heat flow decay in vertical jet of aircraft deicing fluid based on phase field and realizable k-ε turbulence model. *Thermal Science and Engineering Progress,* 60. https://doi.org/10.1016/j.tsep.2025.103446.

[6] Gu, M., Wang, H., Chen, G., Yu, A., Dang, W., & Ling, X. (2024). Experimental and numerical study on explosion resistance of polyurea-coated shelter in petrochemical industry. *Scientific Reports, 14*(1), 20643. https://doi.org/10.1038/s41598-024-71339-w.

[7] Guan, R., Gu, J., Li, Y., Yang, C., Zhang, B., Yao, X., Zhu, R., Wang, Q., Dong, W., & Huang, Y. (2025). Simulation and experimental study of shell-kernel separation device for household sunflower based on CFD-DEM coupling. *Scientific Reports,* 15(1), 9209. https://doi.org/10.1038/s41598-025-93459-7.

[8] Hu, Z., Zeng, H., Ge, Y., Wang, W., & Wang, J. (2021). Simulation and experiment of gas-solid flow in a safflower sorting device based on the CFD-DEM coupling method. *Processes,* 9(7). https://doi.org/10.3390/pr9071239.

[9] Li, H., Niu, H., Zhang, H., & Zhang, M. (2024). Performance evaluation and parameter optimization of a walnut shell–kernel winnowing device. *Journal of Food Process Engineering,* 47(1), e14498. https://doi.org/10.1111/jfpe.14498.

[10] Lundin, S.-T. B., Ikeda, A., & Hasegawa, Y. (2024). On the Maximum Obtainable Purity and Resultant Maximum Useful Membrane Selectivity of a Membrane Separator. *Membranes,* 14(6), 143. https://doi.org/10.3390/membranes14060143.

[11] Luo, W., Jiang, D., Wu, T., Guo, C., Wang, C., Deng, R., & Dai, S. (2020). Numerical simulation of an ice-strengthened bulk carrier in brash ice channel. *Ocean Engineering, 196*, N.PAG.

https://doi.org/10.1016/j.oceaneng.2019.106830.

[12] Ma, H., Zhou, L., Liu, Z., Chen, M., Xia, X., & Zhao, Y. (2022). A review of recent development for the CFD-DEM investigations of non-spherical particles. *Powder Technology,* 412. https://doi.org/10.1016/j.powtec.2022.117972.

[13] Ma, X., Zhao, L., Guo, B., & Dang, H. (2020). Simulation and experiment of rice cleaning in air-separation device based on DEM-CFD coupling method. *INTERNATIONAL JOURNAL OF AGRICULTURAL AND BIOLOGICAL ENGINEERING,* 13(5), 226–233. https://doi.org/10.25165/j.ijabe.20201305.5225.

[14] Michaelides, E. E., & Feng, Z. (2023). Review-Drag Coefficients of Non-Spherical and Irregularly Shaped Particles. *JOURNAL OF FLUIDS ENGINEERING-TRANSACTIONS OF THE ASME,* 145(6), 060801. https://doi.org/10.1115/1.4057019.

[15] Mutinda, E. S., Kimutai, F., Mkala, E. M., Waswa, E. N., Odago, W. O., Nanjala, C., Ndungu, C. N., Gichua, M. K., Njire, M. M., Gituru, R. W., & Hu, G.-W. (2023). Ethnobotanical uses, phytochemistry and pharmacology of pantropical genus Zanthoxylum L. (Rutaceae): An update. *Journal of Ethnopharmacology,* 303. https://doi.org/10.1016/j.jep.2022.115895.

[16] Shi, W.-J., Chai, T., Lv, C.-M., Wang, X.-R., Zhang, X.-R., Qiang, Y., Wang, W.-F., & Yang, J.-L. (2025). Research progress on the main flavor components and detection methods of Zanthoxylum bungeanum Maxim. *Journal of Food Composition and Analysis,* 144. https://doi.org/10.1016/j.jfca.2025.107658.

[17] Stepanenko, S., Kuzmych, A., Shvydia, V., Kotov, B., Kalinichenko, R., Kharchenko, S., Shchur, T., Kocira, S., Kwaśniewski, D., & Dziki, D. (2022). To the Theory of Grain Motion in an Uneven Air Flow in a Vertical Pneumatic Separation Channel with an Annular Cross Section. *Processes,* 10(10). https://doi.org/10.3390/pr10101929.

[18] Ulusoy, U. (2023). A Review of Particle Shape Effects on Material Properties for Various Engineering Applications: From Macro to Nanoscale. *MINERALS,* 13(1), 91. https://doi.org/10.3390/min13010091

[19] Wang, J., Chen, L., Tang, Y., Chen, Z., Wu, Q., & Han, D. (2023). Calibration and experiment of discrete element model parameters of Zanthoxylum bungeanum. *Frontiers in Mechanical Engineering,* 9. https://doi.org/10.3389/fmech.2023.1204659.

[20] Wu, Y., Zheng, Q., Yang, L., & Yu, A. (2025). Coupled CFD-FEM approach for dense particle-fluid flows. *International Journal of Mechanical Sciences,* 308, N.PAG. https://doi.org/10.1016/j.ijmecsci.2025.110985.

[21] Xiao, B., Wang, P., Wu, J., Zhu, H., Liu, M., Liu, Y., & Long, G. (2022). A Novel Fractal Model for Gas Diffusion Coefficient in Dry Porous Media Embedded with a Damaged Tree-Like Branching Network. *Fractals,* 30(7), 1–15. https://doi.org/10.1142/S0218348X2250150X.

[22] Xu, D., Xie, Z., & Shen, Y. (2025). Coarse-grained superquadric DEM-CFD model for gas–solid flow with non-spherical particles. *Chemical Engineering Science,* 315, N.PAG. https://doi.org/10.1016/j.ces.2025.121838.

[23] Zhang, J., Xie, C., Cao, L., Zhou, H., Li, C., & Wang, L. (2022). Determination of physical and interaction parameters of green pepper (Zanthoxylum armatum): Investigation of the mechanism of significant factors against the repose angle. *LWT - Food Science & Technology,* 162, N.PAG. https://doi.org/10.1016/j.lwt.2022.113409.

[24] Zhao, B., Shi, K., He, M., & Wang, J. (2024). Hydrodynamics of polydisperse gas-solid flows: Kinetic theory and multifluid simulation. *Chemical Engineering Science,* 287. https://doi.org/10.1016/j.ces.2024.119740.

[25] Zhao, C., Gao, Q., Chen, Y., & Li, C. (2021). Application of parametric function in construction of particle shape and discrete element simulation. *Powder Technology,* 387, 481–493. https://doi.org/10.1016/j.powtec.2021.04.054.

[26] Zhou, L., Zhao, Z., Li, W., Bai, L., & Agarwal, R. K. (2023). Influence mechanism of particle density in a gas-solid fluidized bed. *PHYSICS OF FLUIDS,* 35(12), 123345. https://doi.org/10.1063/5.0180227.

[27] Zhu, X., Zhang, C., Feng, P., Yang, X., & Yang, X. (2021). A novel pulsated pneumatic separation with variable-diameter structure and its application in the recycling spent lithium-ion batteries. *Waste Management,* 131, 20–30. https://doi.org/10.1016/j.wasman.2021.05.027.